



This is a repository copy of *Effects of inflow conditions on low mass-damping cylinder subjected to vortex-induced vibrations*.

White Rose Research Online URL for this paper:

<https://eprints.whiterose.ac.uk/190624/>

Version: Accepted Version

Article:

Mella, D., Brevis, W. and Susmel, L. (2022) Effects of inflow conditions on low mass-damping cylinder subjected to vortex-induced vibrations. *Ocean Engineering*, 262. 112238. ISSN 0029-8018

<https://doi.org/10.1016/j.oceaneng.2022.112238>

© 2022 Elsevier Ltd. This is an author produced version of a paper subsequently published in *Ocean Engineering*. Uploaded in accordance with the publisher's self-archiving policy. Article available under the terms of the CC-BY-NC-ND licence (<https://creativecommons.org/licenses/by-nc-nd/4.0/>).

Reuse

This article is distributed under the terms of the Creative Commons Attribution-NonCommercial-NoDerivs (CC BY-NC-ND) licence. This licence only allows you to download this work and share it with others as long as you credit the authors, but you can't change the article in any way or use it commercially. More information and the full terms of the licence here: <https://creativecommons.org/licenses/>

Takedown

If you consider content in White Rose Research Online to be in breach of UK law, please notify us by emailing eprints@whiterose.ac.uk including the URL of the record and the reason for the withdrawal request.



eprints@whiterose.ac.uk
<https://eprints.whiterose.ac.uk/>

Highlights

Effects of inflow conditions on low mass-damping cylinder subjected to vortex-induced vibrations

Daniel Mella, Wernher Brevis, Luca Susmel

- Proper inflow conditions on VIV simulations facilitate upper branch response
- Up to 60% computational time per simulation reduction with proper inflow conditions
- Multi-frequency forces interfere fluid-body interaction triggering unstable responses
- Unstable upper to lower branch responses sensitive to 2D RANS model limitations

Effects of inflow conditions on low mass-damping cylinder subjected to vortex-induced vibrations

Daniel Mella^{a,*}, Wernher Brevis^b and Luca Susmel^a

^aDepartment of Civil and Structural Engineering, The University of Sheffield, Sheffield, United Kingdom

^bDepartment of Hydraulics and Environmental Engineering and Department of Mining Engineering, Pontifical Catholic University of Chile, Santiago, Chile

ARTICLE INFO

Keywords:

Fluid-structure interaction
Vortex-induced vibrations
Bifurcation
Inflow velocity
Hysteresis

ABSTRACT

This work analyses the effects of the inflow conditions on the bifurcations characteristics of a two-degree-of-freedom low mass-damping cylinder undergoing vortex-induced vibrations. A two-dimensional RANS model was implemented to simulate the fluid-structure interaction problem. The cylinder response was analysed under different inflow conditions and systematic decrements of the inflow acceleration. The results showed a bifurcated response throughout the upper branch, dependent on the inflow conditions. A low-amplitude state was observed at high inflow accelerations, whereas a high-amplitude state was reached when the inflow acceleration decreased below a certain threshold. A proper selection of the inflow conditions led to a significant increment of the minimum inflow acceleration required to trigger the upper branch, reducing up to 60% of the computational time per simulation. The bifurcated response was divided based on its temporal stability, where the cylinder transitioned from a high- to a low-amplitude state after several high-amplitude oscillations. Unstable responses were associated with multi-frequency fluid forces that interfere with the fluid-cylinder energy transfer, precipitating a state transition. A systematic analysis of the unstable region showed that slight differences in the initial inflow conditions and the inherent simplifications of the tested two-dimensional RANS model significantly impacted the cylinder response stability.

1. Introduction

Technological advances in material properties, construction techniques, and engineering design have led to slender and more flexible structures susceptible to vibrations caused by surrounding fluid flows. A common phenomenon in these cases is vortex-induced vibrations (VIV), which refers to the constant feedback between vortex and body motion (Williamson and Govardhan (2004)). Structures subjected to VIV might experience large oscillations when the structural vibration and vortex shedding frequencies coincide (Bourguet et al. (2011)). This phenomenon is commonly referred to as lock-in or synchronisation and is an important contributor to fatigue damage and structural instability. Several parameters, such as Reynolds number, mass ratio m^* (ratio between the oscillating structure and displaced fluid mass), damping ratio ζ , and degree-of-freedom, have been shown to influence VIV. Khalak and Williamson (1996) tested an elastically mounted cylinder restricted to move in its cross-flow direction (one-degree-of-freedom) and subjected to a range of flow velocities. Cylinders with low $m^*\zeta$ exhibited three distinctive response branches: the initial branch, the upper branch, where the maximum amplitude was achieved, and the lower branch. The initial-upper branch transition exhibited a hysteretic behaviour, whereas an intermittent switching characterised the upper-lower branch transition (Khalak and Williamson (1999)). A systematic analysis of

one-degree-of-freedom cylinders undergoing VIV at different m^* , ζ , and Reynolds numbers can be found in Blevins and Coughran (2009). As the cylinder configuration increases in complexity (e.g. streamwise and crossflow motion or two-degree-of-freedom), unique characteristics in terms of maximum responses (Leong and Wei (2008)), cylinder trajectories (Kheirkhah et al. (2012, 2016); Mella et al. (2020a,b)), and vortex patterns (Jauvtis and Williamson (2004); Fleming and Williamson (2005)) have been observed.

The engineering design of structures subjected to VIV depends on practical and reliable methods to estimate fluid forces, maximum displacements, and oscillation frequencies, among other relevant parameters. Numerical models are becoming increasingly attractive among these methods due to the rapid development in computational power and numerical techniques. Still, the non-linear and hysteretic nature of VIV imposes significant challenges regarding the modelling of turbulent scales as the fluid flow interacts with the structure. Several numerical studies usually circumvent these difficulties by solving the Reynolds-Averaged Navier-Stokes (RANS) equations for the fluid flow and analysing a two-dimensional (2D) representation of the VIV problem. Some of these studies have shown promising results in modelling one-degree-of-freedom (Wanderley and Soares (2015); Zhu and Yao (2015)) and two-degree-of-freedom (Zhao and Cheng (2011); Kang et al. (2017); Han et al. (2018)) cylinders subjected to VIV above the laminar vortex shedding regime. The experimental work of Khalak and Williamson (1996) and Jauvtis and Williamson (2004) are commonly used to validate numerical models with one- and two-degree-of-freedom cylinders, respectively. In particular, Jauvtis and Williamson (2004) observed peak amplitudes of

*Corresponding author. D.A. Mella. Department of Civil and Structural Engineering, The University of Sheffield, Mappin Street, S1 3JD, Sheffield, UK

 daniel.mella@kentplc.com (D. Mella)
ORCID(s): 0000-0003-0642-1300 (D. Mella)

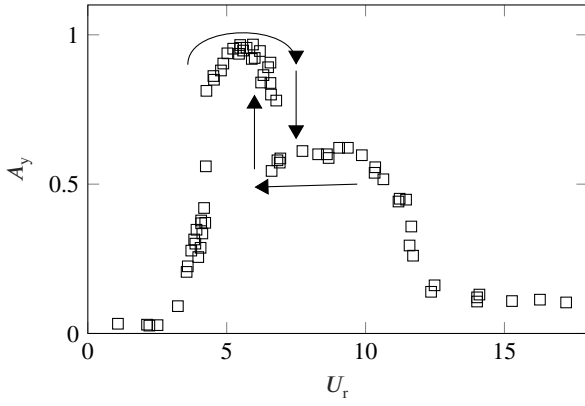


Figure 1: Example of bifurcation in the upper branch of a one-degree-of-freedom cylinder subjected to VIV. Source: Khalak and Williamson (1996)

up to $1.5D$ (D : cylinder diameter) for a low $m^*\zeta$ two-degree-of-freedom cylinder. In addition, the complex vortex pattern 2T (two triplets of vortices per oscillation) was observed in the region of high cylinder amplitudes. This work implements a 2D RANS model to simulate the experimental study of Jauvtis and Williamson (2004).

It is common knowledge that cylinders subjected to VIV exhibit strong bifurcation characteristics near branch transitions (Ni et al. (2019)). Specifically, a cylinder can exhibit different responses as a function of the rate of change of the inflow velocity, amplitude or frequency (Sarpkaya (2004)). A common bifurcation in low $m^*\zeta$ cylinders is observed in the upper branch region, where a low- or high-amplitude response state can be achieved under increasing or decreasing inflow velocities with their respective rate of change per unit of time (Figure 1). Brika and Laneville (1993) tested a flexible cylinder subjected to VIV under decreasing, increasing and impulsive inflow velocities. The upper branch was captured under slow increments of the inflow velocity, while the lower branch appeared under decreasing velocity conditions or when the cylinder was released from rest at a constant inflow velocity. Singh and Mittal (2005) simulated a one- and two-degree-of-freedom cylinder subjected to VIV under increasing and decreasing inflow velocity conditions. The cylinder response showed hysteretic behaviour at both ends of the synchronisation range independent of the degrees of freedom considered. The numerical model of Prasanth et al. (2011) showed a dependence between the hysteretic behaviour of a cylinder undergoing VIV and m^* , ζ , blockage ratio and degree-of-freedom. Ni et al. (2019) simulated experimental case of Jauvtis and Williamson (2004) and applied different displacement perturbations while the cylinder vibrated in the upper branch (called super-upper branch in Jauvtis and Williamson (2004)). The results showed that a proper excitation could trigger a transition from a high-amplitude to a low-amplitude state.

Although the bifurcation characteristics of cylinders subjected to VIV are well documented, the specific inflow conditions that lead to a particular low- or high-amplitude

state are usually not reported and vary widely between the few numerical studies that implicitly describe them. One reason for this lack of information is that measurements in physical experiments are usually taken between small increments/decrements of inflow velocity. In most cases, this systematic approach leads to a high- or low-response state without considering the time history of the inflow velocity. On the contrary, numerical simulations must define and quantify all relevant parameters in advance. Thus, it is critical to define the inflow conditions that correctly lead to a low- and high-response state. Issues regarding the correct selection of the inflow conditions were previously highlighted (Guilmineau and Queutey (2004); Wanderley and Soares (2015)) and might explain some of the major discrepancies between experimental and numerical upper branch responses (e.g. Gao et al. (2018); Gsell et al. (2019)). Kang et al. (2017) analysed the effects of different inflow accelerations on the cylinder response. Each simulation was performed at $U_r = 6$ with successive reductions of the inflow acceleration. Here, $U_r = U_{in}/f_{nw}D$, where U_{in} is the bulk inflow velocity, and f_{nw} is the natural frequency of the structure measured in still water. The cylinder response approached the experimental work of Jauvtis and Williamson (2004) when the inflow velocity was slowly increased for at least 150 seconds. Zhao and Cheng (2011) successfully simulated the upper branch observed in Jauvtis and Williamson (2004) under increasing velocity conditions. Compared with Kang et al. (2017), the simulation started at $U_r = 2$ and was slowly increased for 65 seconds to $U_r = 6$. Similarly, the results of Han et al. (2018) and Wang and Chi (2019) seem to indicate that a high-response state at $U_r = 6$ was achieved when the initial inflow velocity was increased for 40 and 20 seconds, respectively. These different results strongly suggest that the influence of the inflow conditions on the cylinder response is an area that requires further research.

This work analyses the effects of the inflow conditions on the bifurcations characteristics of a two-degree-of-freedom low $m^*\zeta$ cylinder undergoing VIV. A 2D RANS model with the Shear Stress Transport (SST) $k-\omega$ turbulence model and the Runge-Kutta fourth-order algorithm was implemented to simulate the experimental case of Jauvtis and Williamson (2004). The cylinder response was analysed under different inflow conditions and systematic decrements of the inflow acceleration. The response state and stability of the high-amplitude displacement were analysed throughout the upper branch. Limitations regarding 2D RANS models on cylinders undergoing VIV were also highlighted.

2. Numerical method

2.1. Mathematical model and coupling mechanism

The RANS equations for an incompressible viscous flow are

$$\overline{u'_i u'_j} = -\nu_t \left(\frac{\partial u_i}{\partial x_j} + \frac{\partial u_j}{\partial x_i} \right) + \frac{2}{3} k \delta_{ij} \quad (1)$$

where ν_t is the turbulent viscosity, k is the turbulent kinetic energy, and $\delta_{ij} = 1$ when $i = j$. The RANS equations were solved alongside the SST $k - \omega$ turbulence model (Menter (1994); Menter et al. (2003)). This model has shown satisfactory results in one-degree-of-freedom (Wanderley and Soares (2015); Zhu and Yao (2015)) and two-degree-of-freedom (Zhao and Cheng (2011); Kang et al. (2017); Han et al. (2018)) cylinders subjected to VIV. The numerical model was implemented in Ansys Fluent (Fluent (2018)). The following spatial and time discretisation schemes were used: Second order implicit for temporal discretisation, Semi-Implicit Method for Pressure Linked Equations (SIMPLE) for pressure and velocity coupling, Body Force Weighted for pressure, Quadratic Upwind Interpolation for Convection (QUICK) for momentum, first upwind scheme for the dissipation rate, and second upwind scheme for kinetic energy. Convergence was achieved when all flow residuals reached 10^{-5} . These parameters were selected based on previous numerical studies (Han et al. (2018); Wang and Chi (2019)).

The cylinder was modelled as a two-degree-of-freedom mass-damping-spring system

$$M \frac{\partial^2 x}{\partial t^2} + C \frac{\partial x}{\partial t} + Kx = F_x \quad (2)$$

$$M \frac{\partial^2 y}{\partial t^2} + C \frac{\partial y}{\partial t} + Ky = F_y \quad (3)$$

where M , C , and K are the oscillating mass, damping, and stiffness of the system per unit of length, $[x, y]$ is the position of the cylinder in the streamwise (x -axis) and crossflow (y -axis) direction, and $[F_x, F_y]$ are the total drag and lift forces on the cylinder, respectively. The structural properties per unit of length are

$$C = 4\pi f_{na} \zeta M \quad (4)$$

$$K = 4\pi^2 f_{na}^2 M \quad (5)$$

where f_{na} is the natural frequency of the cylinder measured in air. f_{na} and f_{nw} are related as

$$f_{nw} = f_{na} \sqrt{\frac{m^*}{m^* + C_a}} \quad (6)$$

where C_a is the added mass coefficient. $C_a = 1$, as in Jauvtis and Williamson (2004).

A staggered approach with a dynamic mesh deformation algorithm was adopted for the cylinder-fluid coupling mechanism. The RANS equations with the SST $k - \omega$ turbulence model were iteratively solved until convergence. The total pressure and viscous forces on the cylinder were extracted using a User Defined Function. Equations 2 and 3 were

solved using the Runge-Kutta fourth-order algorithm. As the cylinder updates its position, the nearby mesh adapts following a diffusion-based smoothing scheme with a diffusion parameter $\gamma = 1$. Detailed information about this mesh deformation technique can be found in Han et al. (2016).

2.2. Computational domain and mesh

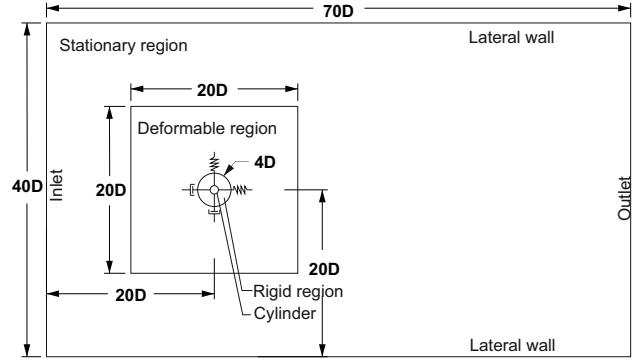


Figure 2: Computational domain. Flow direction from left to right

Figure 2 shows a rectangular domain of $40D$ width and $70D$ length. The chosen width followed the results of Zhao et al. (2012), which found negligible differences in response amplitude when the width domain was higher than $10D$. The origin of the coordinate system was located at the cylinder centreline. The fluid flow entered from the inlet at $20D$ upstream of the cylinder and exited at $50D$ from the origin. The mesh was divided into three regions, as shown in Figure 3. Firstly, a dense O-grid around the cylinder extends $4D$ from the origin. This region moved with the cylinder to preserve its shape. Secondly, a square-shaped grid of quadrilateral elements absorbed the cylinder motion by deforming its mesh elements. Thirdly, a stationary region. The upper and lower walls were set to free-slip boundaries, while a no-slip condition was used at the cylinder surface. The inlet boundary had a time-dependent streamwise velocity. The outlet had a reference pressure equal to zero.

The High Performance Computing cluster at the University of Sheffield was used to request multiple nodes and perform several simulations simultaneously. The computational time was limited by 96 hours per requested node. Each node had the following computational resources: Dell PowerEdge C6320 with $2 \times 2.40\text{GHz}$ Intel Xeon E5-2630 v3 and 64 GB of DDR4 RAM.

3. Numerical set-up

3.1. Experimental Parameters

This work simulated the experimental case of Jauvtis and Williamson (2004). A two-degree-of-freedom cylinder was subjected to a range of Reynolds numbers between $1.4 \times 10^3 \leq Re \leq 1 \times 10^4$. $Re = U_{in} D / \nu$, where ν is the kinematic viscosity of water. Relevant structural parameters

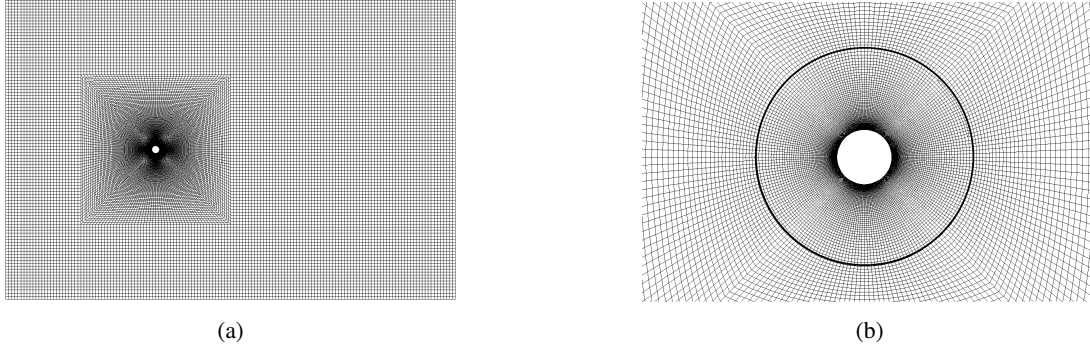


Figure 3: Mesh configuration scheme. (a) Mesh domain. (b) Mesh around cylinder

are: $D = 0.0381$ m, $f_{nw} = 0.4$ Hz, $m^* = 2.6$, $\zeta = 0.00361$, and $f_{na} = 0.47$ Hz as per Equation 6. The experimental turbulent intensity was 0.9% with an estimated turbulent length scale of $0.04D$, as in Han et al. (2018).

3.2. Inflow conditions

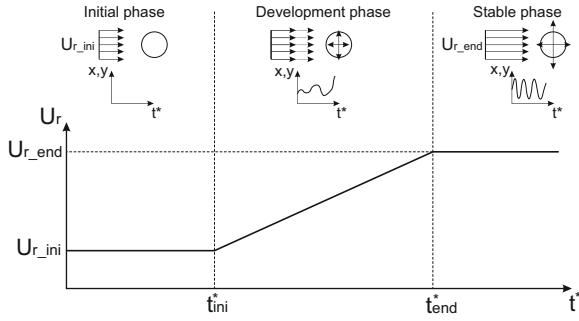


Figure 4: Increasing inflow velocity condition

The time history of the inflow velocity was divided into three phases (Figure 4). Firstly, the initial phase, where the cylinder was fixed and subjected to U_{r_ini} for an initial time t_{ini}^* . Throughout this work, all time units with the superscript (*) were normalised by f_{nw} , $t^* = tf_{nw}$, for example. Secondly, the development phase, where a freely vibrating cylinder is subjected to an accelerating inflow velocity $U_{r_ini} + a_c(t^* - t_{ini}^*)$ for an acceleration time t_a^* . Thirdly, the stable phase, where the inflow velocity reached U_{r_end} and was maintained until at least 20 stable oscillations were recorded. $t_{ini}^* = 0$ results in a freely vibrating cylinder throughout the entire simulation. $t_a^* = 0$ results in a constant inflow velocity condition. The normalised acceleration was defined as

$$a_c = \frac{U_{r_end} - U_{r_ini}}{t_a^*} \quad (7)$$

where $t_a^* = t_{end}^* - t_{ini}^*$. The minimum acceleration time required to trigger the upper branch was t_{trig}^* . Conversely, the maximum normalised acceleration required to reach a high-amplitude state was a_{trig} .

4. Model validation and computational time analysis

The accuracy of four mesh resolutions (M1 to M4) was analysed under different inflow conditions. The mesh resolution was controlled by the total number of mesh elements N_e , the number of elements around the cylinder N_c , the number of layers N_L and growth rate g_r in the radial direction within the O-grid zone, and the height of the first element around the cylinder H_{y+} . Each simulation started at $U_{r_ini} = 2$ and was slowly increased for $t_a^* = 25$ until $U_{r_end} = 5$ or $U_{r_end} = 6$ was reached. A time step of 0.0015 s was used to ensure a Courant-Friedrichs-Lewy number of less than one.

The accuracy of each simulation was assessed in terms of maximum cylinder displacement in the streamwise A_x and crossflow A_y direction, root-mean-square (rms) drag $C_{D,rms}$ and lift $C_{L,rms}$ coefficients, and oscillation frequency in the crossflow direction f_y . Each parameter was calculated using the last 20 oscillations within the stable phase. The cylinder response and oscillation frequency were normalised by D and f_{nw} , respectively. Similarly, the force coefficients were normalised by $\rho_w D (U_{r_ini} f_{nw} D)^2$, where ρ_w is the water density. Table 1 summarises the results alongside previous numerical studies. The M1 case predicted a highly modulated response at $U_{r_end} = 5$. This irregular response dissipated as the mesh resolution increased, reaching a stable high-amplitude response in the M3 and M4 cases. On the other hand, good agreement across mesh resolutions was achieved at $U_{r_end} = 6$. Comparing the M3 and M4 cases with Jauvtis and Williamson (2004), the maximum amplitude and force coefficients were over-predicted at $U_{r_end} = 5$, whereas A_y and $C_{L,rms}$ were 9.3% and 15.1% lower at $U_{r_end} = 6$, respectively. The oscillation frequency was properly captured across tested conditions. Overall, the accuracy of the numerical model is comparable to previous numerical studies. From now on, M3 mesh is used as a compromise between accuracy and required computational time per simulation (25% lower than M4).

The total computational time (TCT) per simulation was used to compare the computational costs associated with cases under different inflow conditions. This parameter was estimated from the average time per iteration and the total

Case	N_e	N_c	N_L	g_r	H_{y^+}	$U_r = 5$					$U_r = 6$				
						A_x	A_y	f_y	$C_{D,rms}$	$C_{L,rms}$	A_x	A_y	f_y	$C_{D,rms}$	$C_{L,rms}$
M1	7840	80	40	1.15	0.00075D	-	-	-	-	-	0.2	0.96	0.92	1.16	1.91
M2	16260	120	56	1.11	0.00053D	0.03	0.73	0.92	0.46	1.98	0.2	0.97	0.92	1.18	1.87
M3	26270	160	63	1.1	0.00053D	0.06	0.73	0.84	0.46	1.87	0.19	0.98	0.92	1.11	1.79
M4	41300	200	81	1.08	0.00039D	0.06	0.72	0.84	0.49	1.85	0.18	0.97	0.92	1.09	1.76
Num1	-	226800	160	-	-	-	-	-	-	-	0.17	1.07	0.87	1.52	1.2
Num2	-	42761	200	-	0.003D	-	-	-	-	-	0.15	1.14	0.93	1.14	1.71
Exp.	-	-	-	-	-	0.03	0.54	0.86	0.13	1.53	0.19	1.08	0.89	1.00	2.06

Table 1

Mesh sensitivity analysis. N_e : Number of mesh elements. N_c : Number of elements around the cylinder. N_L : Number of O-grid layers. g_r : O-grid growth rate. H_{y^+} : Height of the first element around the cylinder. Num1: Han et al. (2018). Num2: Wang et al. (2018). Exp: Jauvtis and Williamson (2004)

Case	$a_c = 0.5$				$a_c = 0.38$			
	IP	DP	SP	TCT	IP	DP	SP	TCT
M1	1.39	3.35	6.79	11.53	1.42	9.06	7.00	17.47
M2	1.62	6.16	10.62	18.40	1.69	14.16	10.97	26.83
M3	3.57	8.98	15.40	27.96	3.39	20.54	14.28	38.20
M4	4.57	11.91	20.61	37.10	4.35	27.48	19.12	50.96

Table 2

Computational time in hours at $U_r = 6$. IP: initial phase. DP: development phase. SP: stable phase. TCT: total computational time

number of iterations per time step. The initial and development phases were delimited by t_{ini}^* and t_{end}^* , respectively. The computational time of the stable phase started at t_{end}^* and included 30 response oscillations to account for transient responses between phases. Table 2 shows the computational time per inflow velocity phase and mesh resolution of two cases with different normalised accelerations. As expected, the TCT increases at higher mesh resolutions. More importantly, the computational time of the development phase accounted for 31.7% and 53.1% of the TCT at $a_c = 0.5$ and $a_c = 0.38$, respectively. These results show that the development phase becomes more dominant in proportion to the TCT as the inflow velocity decreases. As shown later, a proper selection of the inflow conditions can reduce the computational time of the development phase and substantially decrease the required computational time per simulation.

5. Results and analysis

5.1. Initial phase

The effects of the initial phase on the cylinder response were analysed at different t_{ini}^* and $U_{r,ini}$. Three cases were considered based on the temporal evolution of the lift and drag forces around the cylinder (Figure 5): $t_{ini}^* = 0$ (cylinder is free to move throughout the simulation), $t_{ini}^* = 24$ (cylinder is released while the fluid forces are developing), and $t_{ini}^* = 60$ (cylinder is released when the fluid forces reached a steady oscillatory state). Each case started from $U_{r,ini} = 2$ (Zhao and Cheng (2011)) to $U_{r,end} = 6$ with $0 \leq t_a^* \leq 24$. Figure 6 shows the maximum crossflow amplitude and oscillation frequency for each tested inflow condition. Two response states are clearly identified. A low-amplitude state, where $A_y = 0.57$ and $f_c/f_{nw} = 1.3$, and a

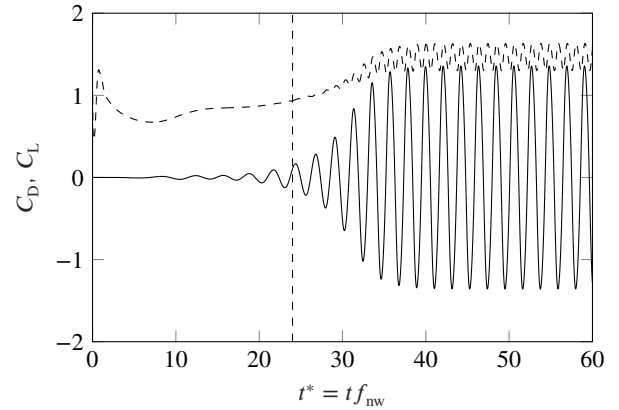


Figure 5: Total drag (dashed line) and lift force coefficients within the initial phase ($U_{r,ini} = 2$, $R_e = 1.16 \times 10^3$). Vertical dashed line: $t_{ini}^* = 24$

high-amplitude state, where $A_y = 0.98$ and $f_c/f_{nw} = 0.92$. Figure 6a shows an example of each state. Figures 6b and 6c show a sudden response transition from a low- to a high-amplitude state as a_c (t_a^*) decreased (increased). This state shift, observed even under systematic increments of $\Delta t_a^* = 8 \times 10^{-4}$, is in contrast to the smooth transition reported in Kang et al. (2017). The initial and development phases within each state have a negligible impact on the cylinder response. Moreover, the cylinder response stabilised to a specific low- or high-amplitude state throughout the simulation. The minimum inflow acceleration required to trigger the upper branch increased with the initial time. Specifically, $a_{trig} = [0.37, 0.53, 1.43]$ for $t_{ini}^* = [0, 24, 60]$, respectively.

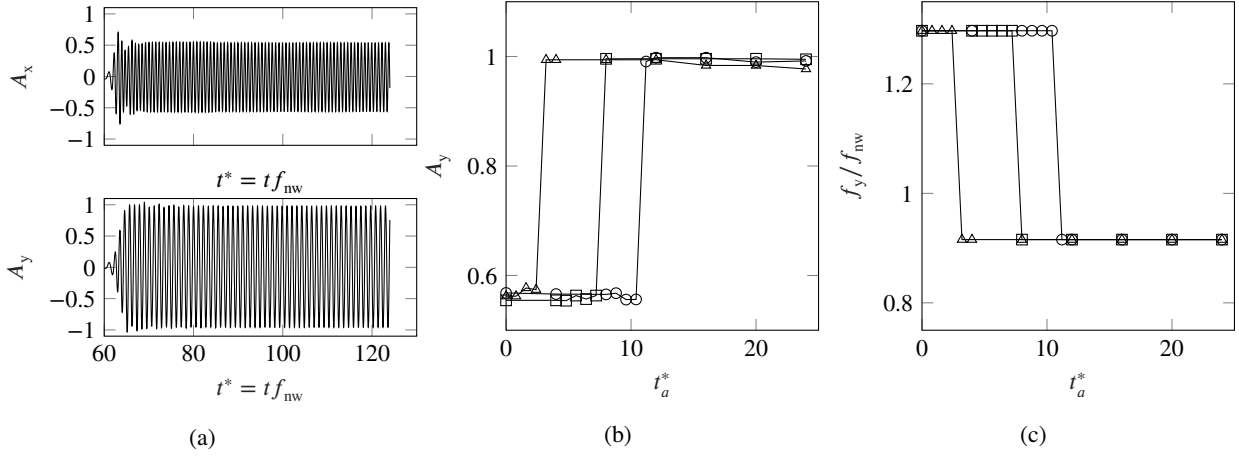


Figure 6: Effects of the initial time on the cylinder response at $U_{r_ini} = 2$ and $U_{r_end} = 6$. a) Time history of the crossflow response at $a_c = 1.88$ (up) and $a_c = 1.5$ (down). Maximum cylinder amplitude (b) and main oscillation frequency (c) at \circ : $t_{ini}^* = 0$, \square : $t_{ini}^* = 24$, and \triangle : $t_{ini}^* = 60$

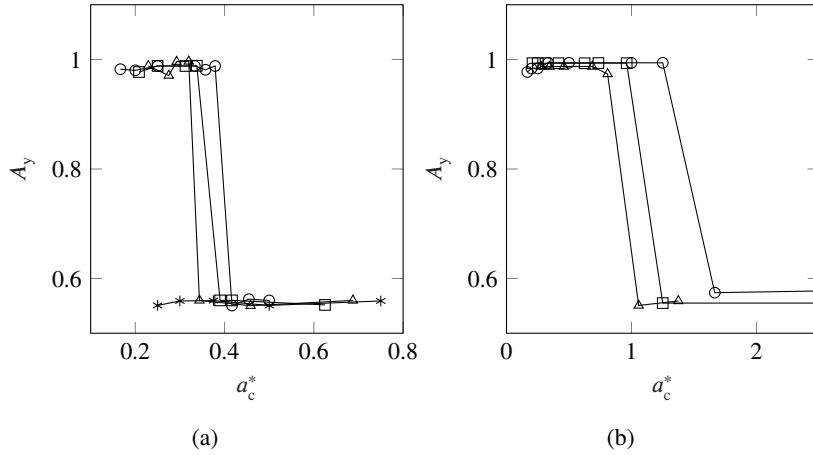


Figure 7: Effects of the initial velocity on the cylinder response at $U_{r_end} = 6$. Maximum cylinder amplitude (a) without initial time ($t_{ini}^* = 0$) and (b) with an initial time that ensured steady oscillatory drag and lift forces ($t_{ini}^* \ge 60$). \circ : $U_{r_ini} = 2$, \square : $U_{r_ini} = 1$, \triangle : $U_{r_ini} = 0.5$. *: $U_{r_ini} = 0$

These results show that the inflow acceleration can be increased up to four times when the fluid forces around the cylinder are allowed to reach a steady oscillatory state within the initial phase.

Previous numerical simulations were performed at $U_{r_ini} = 2$, as in Zhao and Cheng (2011). Next, the effects of the initial reduced velocity were analysed under two conditions: without an initial phase ($t_{ini}^* = 0$), and with an initial phase that ensured steady oscillatory fluid forces ($t_{ini}^* \ge 60$). Figure 7 shows the maximum cylinder amplitude at $U_{r_ini} = [0, 0.5, 1, 2]$; f_y is not shown since it follows A_y . As expected, a_{trig} increases with U_{r_ini} . Figure 7a shows a 10.5% reduction in a_{trig} between the $U_{r_ini} = 2$ and $U_{r_ini} = 0.5$ cases. Likewise, Figure 7b shows a 35.3% decrement in a_{trig} for the same U_{r_ini} difference. The inflow condition $t_{ini}^* = 0$ and $U_{r_ini} = 0$, i.e. flow at rest, did not trigger a high-amplitude state across tested inflow accelerations. Since there is no initial phase, the lift and drag forces must develop under a freely vibrating cylinder and accelerating flow

condition. Thus, an extremely low normalised acceleration is required to minimise disturbances in the fluid-cylinder energy transfer and trigger a high-amplitude state.

Figures 6 and 7 show the influence of the inflow conditions on the cylinder response and its impact on the appearance of a particular low- or high-amplitude state. The minimum acceleration required to trigger the upper branch is significantly increased when the fluid forces around the cylinder are allowed to reach a steady oscillatory state within the initial phase. Previous numerical studies might have chosen initial conditions ($t_{ini}^* = 0$ or $U_{r_ini} = 0$) that required low inflow acceleration to simulate the upper branch and might explain the observed differences in terms of a_{trig} (e.g. $0.07 \leq a_c \leq 0.17$ for Zhao and Cheng (2011); Kang et al. (2017); Ni et al. (2019)). Still, different model parameters and solver strategies might be another source of discrepancy that requires further research. Overall, the reduction in computational time due to a proper consideration of the inflow conditions can help numerical VIV models with strong

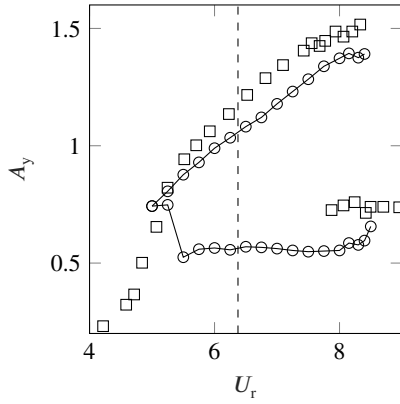


Figure 8: Upper branch bifurcation. Vertical dashed line separates the stable (left) and unstable (right) region. \square : Jauvtis and Williamson (2004)

bifurcation characteristics, where multiple simulations are required to capture the full range of structural responses.

5.2. Bifurcation characteristics in the upper branch

The cylinder response within the upper branch was analysed under different inflow conditions ($U_{r_ini} = 2$, $t_{ini}^* = [0, 60]$) with acceleration times that ranged between $0 \leq t_a^* \leq 32$, as in Section 5.1. Figure 8 summarises the maximum amplitude across reduced velocities. The results of Jauvtis and Williamson (2004) were also plotted for comparison. $U_{r_end} = 5$ marks the beginning of the upper branch, evidenced by the same maximum amplitude ($A_y = 0.57$) independent of the tested inflow conditions. At higher reduced velocities, the cylinder response bifurcated towards a low- or high-amplitude state depending on the initial and development phases. The low-amplitude state maintained an approximately constant $A_y = 0.57$ throughout the upper branch region, whereas the high-amplitude state response increased with U_{r_end} . The numerical model predicted a maximum $A_y = 1.39$ at $U_{r_end} = 8.4$, which is 8% lower than Jauvtis and Williamson (2004). A low-response state was observed at $U_{r_end} = 8.5$ across all tested inflow conditions, indicating a transition to the lower branch.

The observed bifurcation in Figure 8 can be further decomposed in terms of state stability. A bistable response was observed between $5.25 \leq U_{r_end} \leq 6.25$, where a particular low- or high-amplitude state was sustained for the entire duration of the numerical simulation. The results in Section 5.1 apply to this region. Unstable responses under specific inflow conditions were observed at $U_{r_end} = [6.5, 6.75]$, where the cylinder transitioned from a high- to a low-amplitude state after a certain number of vibrations. These unstable responses dominated at $U_{r_end} \geq 7$ across tested inflow conditions. It is important to mention that a motion history is considered stable if a particular response state is maintained for $t^* \geq 50$ after its development phase. The bistable region achieves this criterion

for all tested inflow conditions. However, a particular high-amplitude state within the unstable region might transition to a low-response state beyond the maximum TCT limited by the High Performance Computing cluster (Section 2.1). An example of an unstable cylinder response is shown in Figure 9 for $U_{r_ini} = 2$, $t_{ini}^* = 60$, $a_c = 0.36$, and $U_{r_end} = 7$. The cylinder transitioned to a low-amplitude state after $t^* = 109$ or 32 high-amplitude oscillations (Figure 9a). This transition was accompanied by a drastic change in fluid forces (Figure 9b), resulting in a counter-phase jump between the crossflow motion and lift force (Figure 9c). Pastrana et al. (2018) analysed this high- to low-amplitude state transition using a three-dimensional Large Eddy Simulation model. The researchers observed a multi-vortex shedding pattern followed by an out-of-phase 2T vortex mode at the last high-amplitude oscillation. This complex interaction destabilised the vortex-motion timing, triggering a transition to the stable counter-phase low-amplitude state. A similar phenomenon is observed here. The unstable region is associated with multi-frequency fluid forces that interfere with the vortex strength and fluid-cylinder energy transfer (Sarpkaya (2004)), precipitating a high- to a low-amplitude state transition. Pastrana et al. (2018) identified unstable responses at $U_{r_end} = 6.7$, whereas the tested 2D RANS model predicted them at $U_{r_end} = 6.5$. These results are lower than the intermittent region ($7.9 \leq U_{r_end} \leq 8.3$) observed in Jauvtis and Williamson (2004). More research is needed to understand and predict the stability of the cylinder response near branch transitions.

The stability of the high-amplitude state was quantified as the ratio between the number of high-amplitude oscillations after the development phase (P_{uns}) and the number of oscillations of an equivalent high-amplitude state maintained throughout the entire numerical simulation (P_{ideal}). A low P_{uns}/P_{ideal} ratio indicates a fast high- to low-amplitude state transition, whereas a high P_{uns}/P_{ideal} value implies several high-amplitude oscillations before experiencing a state transition. The total cylinder stability S for a particular inflow condition is

$$S = \frac{\sum_{i=1}^N P_{uns_i}}{\sum_{i=1}^N P_{ideal_i}} \quad (8)$$

where $N = [1, 2, \dots]$ accounts for the different tested a_c .

Figure 10a shows the total cylinder stability across the unstable upper branch region. The initial conditions were $U_{r_ini} = 2$ and $t_{ini}^* = [0, 60]$. The total stability reaches a maximum and minimum value at the start and towards the end of the upper branch, respectively. Although the tested inflow conditions follow the same trend, there are significant changes in total stability across U_{r_end} . Figure 10b exemplifies these differences at $U_{r_end} = 7$. The stability ratio jumped from 7% to 71% over a small a_c increment. Further tests at lower initial velocities ($U_{r_ini} = [0.5, 1]$) showed similar jumps in P_{uns}/P_{ideal} as well. These results show that the initial and development phases have an important influence on the stability of the cylinder response. Another conflating

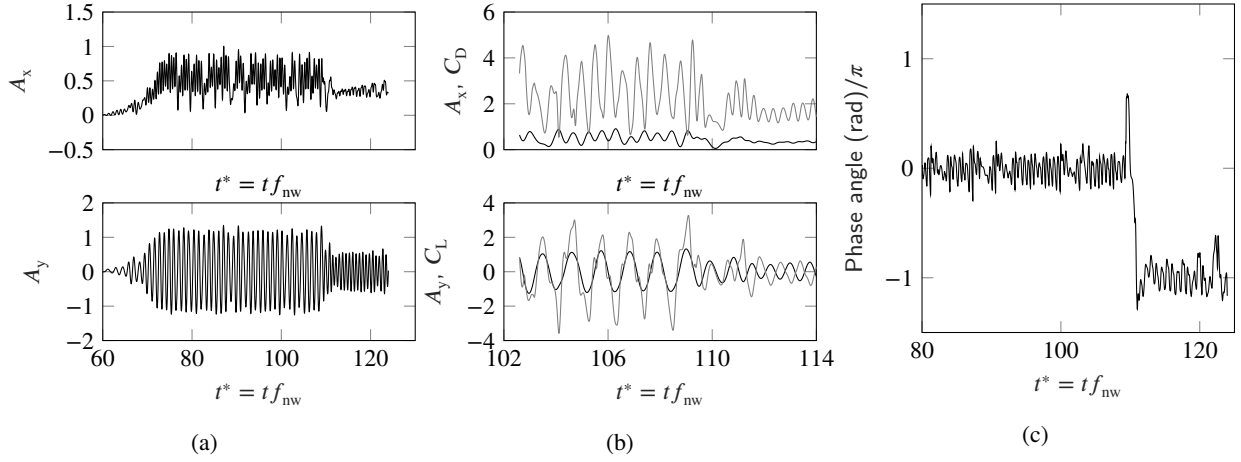


Figure 9: Unstable response at $U_{r,end} = 7$, $t_{ini}^* = 60$ and $a_c = 0.36$. a) streamwise (up) and crossflow (down) displacement. b) drag (up) and lift (down) forces alongside the streamwise and crossflow displacement (black line) near state transition. c) instantaneous phase angle in the crossflow direction

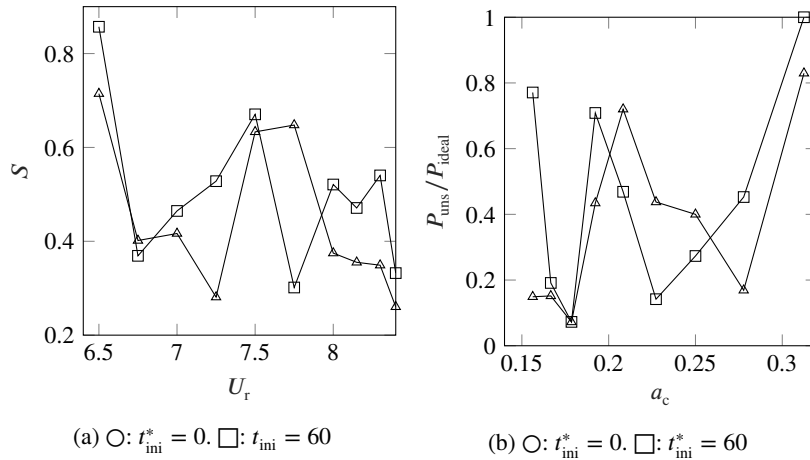


Figure 10: Stability analysis throughout the unstable upper branch region. a) total stability S ($U_{r,ini} = 2$ and $t_{ini}^* = [0, 60]$). b) stability at $U_{r,end} = 7$ across tested a_c

possibility points towards the numerical model as a source of instability. This hypothesis was tested by repeating ten times the $U_{r,end} = [6.5, 6.75, 7]$ cases with $U_{r,ini} = 2$ and $t_{ini}^* = 0$. Figure 11 highlights the highest differences between tested simulations. Ni et al. (2019) indicated that an important source of error near branch jumps could be explained by the inherent simplifications of the RANS equations. This work shows that the tested numerical model is susceptible to these simplifications and round-off numerical errors, which, in turn, influence the upper branch stability.

The relationship between a_{trig} (or t_{trig}^*) and the initial phase is critical to optimise the inflow parameters that lead to a high-response state. It was not possible to establish this relationship due to limitations regarding the maximum TCT per simulation (Section 2.1) and inherent numerical errors of the 2D RANS model. Nevertheless, a simple fit in the stable region at $U_{r,ini} = [0.5, 1, 2]$ resulted in the following relationships

$$t_{trig}^* = (1.55U_{r,end} - U_{r,ini}^{0.9})^{1.65} \quad (9)$$

for $t_{ini}^* = 0$ seconds, and

$$t_{trig}^* = (0.6U_{r,end} - U_{r,ini}^{0.5})^{2.6} \quad (10)$$

for $t_{ini}^* \geq 60$ seconds. The maximum error is $t_{trig}^* \pm 1.2$. This data can be used as a starting point to further research regarding the effects of the inflow conditions that lead to high-response states under changes in Re , $m^*\zeta$, and degree-of-freedom, among other relevant parameters.

6. Conclusions

This work analyses the effects of the inflow conditions on the bifurcations characteristics of a two-degree-of-freedom low mass-damping cylinder undergoing VIV. A 2D RANS

Inflow condition effect on cylinder subjected to VIV

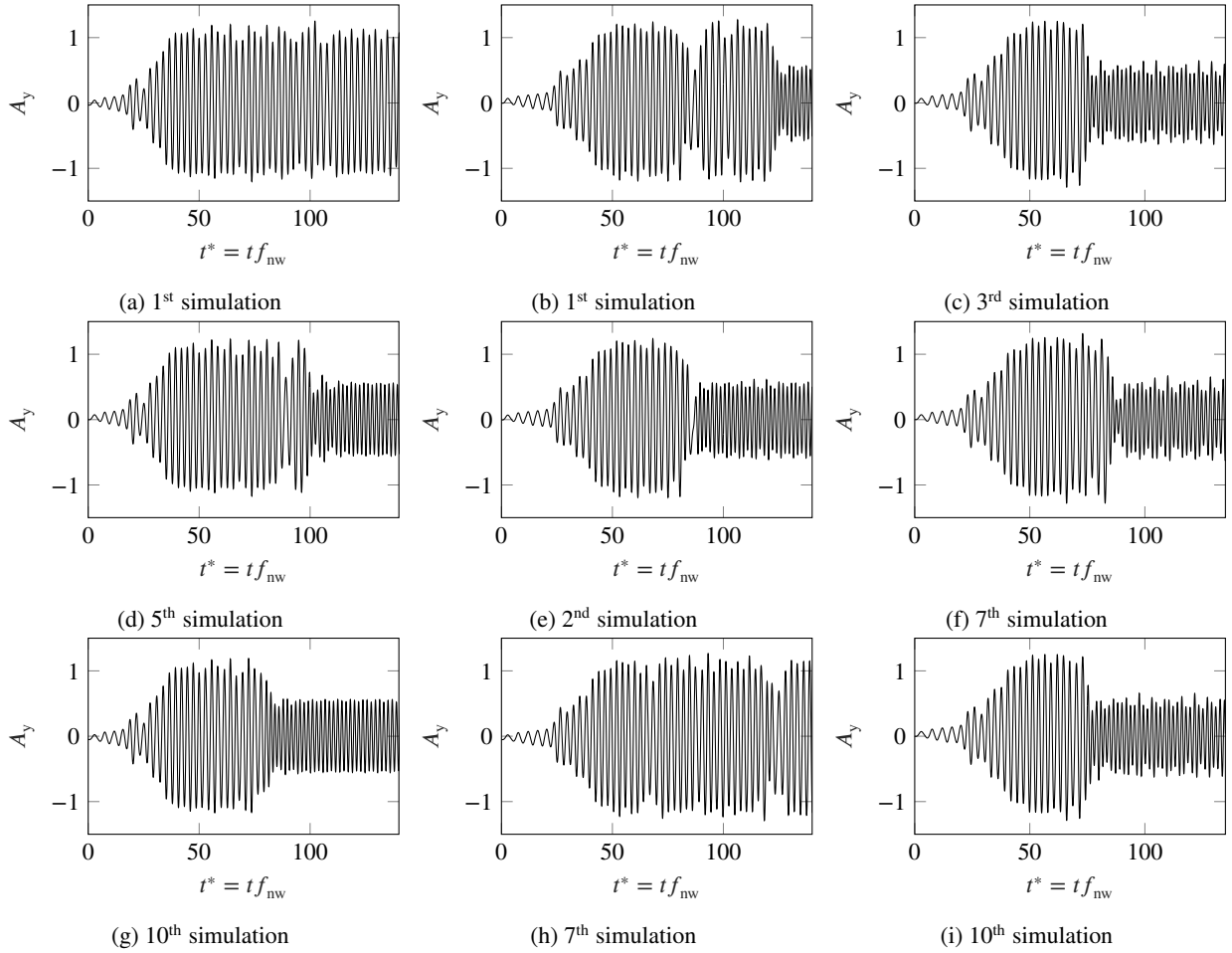


Figure 11: Three cases simulated 10 times each under the same initial conditions ($U_{r,ini} = 2$, $t_{ini}^* = 0$). Only highest differences in crossflow response are shown. (a,d,g) $U_{r,end} = 6.5$. (b,e,h) $U_{r,end} = 6.75$. (c,f,i) $U_{r,end} = 7$

model with the SST $k - \omega$ turbulence model and the Runge-Kutta fourth-order algorithm was implemented to simulate the fluid-structure interaction problem. The cylinder response was analysed under different inflow conditions and systematic decrements of the inflow acceleration. The results showed a bifurcated response throughout the upper branch dependent on the initial inflow conditions. A low-amplitude state was observed at high inflow accelerations, whereas a high-amplitude state was reached when the inflow acceleration decreased below a certain threshold. The transition between amplitude states was affected by the initial phase. The maximum inflow acceleration required to reach a high-amplitude state was increased up to four times when the fluid forces around the cylinder were allowed to reach a steady oscillatory state within the initial phase. A further, although secondary, increment in inflow acceleration can be achieved by considering higher initial reduced velocities. A proper selection of the inflow conditions led to a 60% reduction in the required computational time per simulation.

The bifurcated response within the upper branch can be further decomposed in terms of its temporal stability. A bistable response was observed between $5.25 \leq U_r < 6.25$,

where a particular low- or high-amplitude state was sustained for the duration of the numerical simulation. Unstable responses were observed between $6.5 \leq U_r \leq 8.4$, where the cylinder transitioned from a high- to a low-response state after a certain number of high-amplitude oscillations. Unstable responses were associated with multi-frequency fluid forces that interfere with the vortex strength and fluid-cylinder energy transfer, precipitating a high- to a low-amplitude state transition. A systematic analysis of the unstable region showed that the timing of the amplitude state transition is highly sensitive to the initial inflow conditions and the inherent simplifications of the tested 2D RANS model.

Practical recommendations for 2D RANS models in two-degree-of-freedom low $m^* \zeta$ cylinders subjected to VIV:

- Estimate the range of high-amplitude responses and simulate a particular condition under different inflow accelerations.
- Consider the implementation of an initial phase to significantly increase the minimum inflow acceleration required to trigger a high-amplitude state and, as a consequence, reduce the required computational time per simulation.

- Awareness of possible instabilities in 2D RANS models. Special attention should be taken in cases with low response stability that might be misinterpreted as a low-amplitude state.

Acknowledgement

Work supported by a Doctoral Scholarship from CONICYT/ Concurso para Beca de Doctorado en el Extranjero.

References

- Blevins, R.D., Coughran, C.S., 2009. Experimental Investigation of Vortex-Induced Vibration in One and Two Dimensions With Variable Mass, Damping, and Reynolds Number. *Journal of Fluids Engineering* 131, 101202. doi:10.1115/1.3222904.
- Bourguet, R., Karniadakis, G.E., Triantafyllou, M.S., 2011. Lock-in of the vortex-induced vibrations of a long tensioned beam in shear flow. *Journal of Fluids and Structures* 27, 838–847. doi:10.1016/j.jfluidstructs.2011.03.008.
- Brika, D., Laneville, A., 1993. Vortex-induced vibrations of a long flexible circular cylinder. *Journal of Fluid Mechanics* 250, 481–508. doi:10.1017/S0022112093001533.
- Flemming, F., Williamson, C., 2005. Vortex-induced vibrations of a pivoted cylinder. *Journal of Fluid Mechanics* 522, 215–252. doi:10.1017/S0022112004001831.
- Fluent, A., 2018. *Ansys Fluent Theory Guide*.
- Gao, Y., Zong, Z., Zou, L., Takagi, S., Jiang, Z., 2018. Numerical simulation of vortex-induced vibration of a circular cylinder with different surface roughnesses. *Marine Structures* 57, 165–179. doi:10.1016/j.marstruc.2017.10.007.
- Gsell, S., Bourguet, R., Braza, M., 2019. One- versus two-degree-of-freedom vortex-induced vibrations of a circular cylinder at $Re=3900$. *Journal of Fluids and Structures* 85, 165–180. doi:10.1016/j.jfluidstructs.2019.01.006.
- Guilmineau, E., Queutey, P., 2004. Numerical simulation of vortex-induced vibration of a circular cylinder with low mass-damping in a turbulent flow. *Journal of Fluids and Structures* 19, 449–466. doi:10.1016/j.jfluidstructs.2004.02.004.
- Han, X., Lin, W., Wang, D., Qiu, A., Feng, Z., Tang, Y., Wu, J., 2018. Numerical simulation of super upper branch of a cylindrical structure with a low mass ratio. *Ocean Engineering* 168, 108–120. doi:10.1016/j.oceaneng.2018.09.014.
- Han, X., Lin, W., Zhang, X., Tang, Y., Zhao, C., 2016. Two degree of freedom flow-induced vibration of cylindrical structures in marine environments: frequency ratio effects. *Journal of Marine Science and Technology (Japan)* 21, 479–492. doi:10.1007/s00773-016-0370-5.
- Jauvtis, N., Williamson, C., 2004. The effect of two degrees of freedom on vortex-induced vibration at low mass and damping. *Journal of Fluid Mechanics* 509, 23–62. doi:10.1017/S0022112004008778.
- Kang, Z., Ni, W., Sun, L., 2017. A numerical investigation on capturing the maximum transverse amplitude in vortex induced vibration for low mass ratio. *Marine Structures* 52, 94–107. doi:10.1016/j.marstruc.2016.11.006.
- Khalak, A., Williamson, C., 1996. Dynamics of a hydroelastic cylinder with very low mass and damping. *Journal of Fluids and Structures* 10, 455–472. doi:10.1006/jfls.1996.0031.
- Khalak, A., Williamson, C., 1999. Motions, forces and vortex mode transitions in vortex-induced vibrations at low mass-damping. *Journal of Fluids and Structures* 13, 813–851. doi:10.1006/jfls.1999.0236.
- Kheirikhah, S., Yarusevych, S., Narasimhan, S., 2012. Orbiting response in vortex-induced vibrations of a two-degree-of-freedom pivoted circular cylinder. *Journal of Fluids and Structures* 28, 343–358. doi:10.1016/j.jfluidstructs.2011.08.014.
- Kheirikhah, S., Yarusevych, S., Narasimhan, S., 2016. Wake Topology of a Cylinder Undergoing Vortex-Induced Vibrations With Elliptic Trajectories. *Journal of Fluids Engineering* 138, 054501. doi:10.1115/1.4031971.
- Leong, C.M., Wei, T., 2008. Two-degree-of-freedom vortex-induced vibration of a pivoted cylinder below critical mass ratio. *Proceedings of the Royal Society A: Mathematical, Physical and Engineering Sciences* 464, 2907–2927. doi:10.1098/rspa.2007.0166.
- Mella, D., Brevis, W., Susmel, L., 2020a. Single cylinder subjected to vortex-induced vibrations: Estimating cyclic stresses for fatigue assessment. *Procedia Structural Integrity* 28, 511–516. doi:10.1016/j.prostr.2020.10.060.
- Mella, D., Brevis, W., Susmel, L., 2020b. Spanwise wake development of a bottom-fixed cylinder subjected to vortex-induced vibrations. *Ocean Engineering* 218, 108280. doi:10.1016/j.oceaneng.2020.108280.
- Menter, F.R., 1994. Two-equation eddy-viscosity turbulence models for engineering applications. *AIAA Journal* 32, 1598–1605. doi:10.2514/3.12149.
- Menter, F.R., Kuntz, M., Langtry, R., 2003. Ten Years of Industrial Experience with the SST Turbulence Model. *Turbulence, Heat and Mass Transfer* 4, 625–632.
- Ni, W., Zhang, X., Xu, F., Zhang, W., Kang, Z., 2019. Numerical investigation of bifurcation characteristics under perturbations in vortex induced vibration of cylinder with two degrees of freedom. *Ocean Engineering* 188, 106318. doi:10.1016/j.oceaneng.2019.106318.
- Pastrana, D., Cajas, J.C., Lehmkuhl, O., Rodríguez, I., Houzeaux, G., 2018. Large-eddy simulations of the vortex-induced vibration of a low mass ratio two-degree-of-freedom circular cylinder at subcritical Reynolds numbers. *Computers and Fluids* 173, 118–132. doi:10.1016/j.compfluid.2018.03.016.
- Prasanth, T.K., Premchandran, V., Mittal, S., 2011. Hysteresis in vortex-induced vibrations: Critical blockage and effect of m^* . *Journal of Fluid Mechanics* 671, 207–225. doi:10.1017/S0022112010005537.
- Sarpkaya, T., 2004. A critical review of the intrinsic nature of vortex-induced vibrations. *Journal of Fluids and Structures* 19, 389–447. doi:10.1016/j.jfluidstructs.2004.02.005.
- Singh, S.P., Mittal, S., 2005. Vortex-induced oscillations at low Reynolds numbers: Hysteresis and vortex-shedding modes. *Journal of Fluids and Structures* 20, 1085–1104. doi:10.1016/j.jfluidstructs.2005.05.011.
- Wanderley, J.B., Soares, L.F.N., 2015. Vortex-induced vibration on a two-dimensional circular cylinder with low Reynolds number and low mass-damping parameter. *Ocean Engineering* 97, 156–164. doi:10.1016/j.oceaneng.2015.01.012.
- Wang, K., Chi, Q., 2019. Numerical simulation of the two-degree-of-freedom vortex induced vibration of a circular cylinder at Reynolds number of $O(104-105)$. *Journal of Marine Engineering and Technology* 1, 1–10. doi:10.1080/20464177.2019.1633222.
- Wang, K., Ji, C., Chi, Q., Wu, H., 2018. Hydrodynamic force investigation of a rigid cylinder under the coupling CF and IL motion. *Journal of Fluids and Structures* 81, 598–616. doi:10.1016/j.jfluidstructs.2018.06.004.
- Williamson, C., Govardhan, R., 2004. Vortex-induced vibrations. *Annual Review of Fluid Mechanics* 36, 413–455. doi:10.1146/annurev.fluid.36.050802.122128.
- Zhao, M., Cheng, L., 2011. Numerical simulation of two-degree-of-freedom vortex-induced vibration of a circular cylinder close to a plane boundary. *Journal of Fluids and Structures* 27, 1097–1110. doi:10.1016/j.jfluidstructs.2011.07.001.
- Zhao, M., Tong, F., Cheng, L., 2012. Numerical simulation of two-degree-of-freedom vortex-induced vibration of a circular cylinder between two lateral plane walls in steady currents. *Journal of Fluids Engineering* 134, 104501. doi:10.1115/1.4007426.
- Zhu, H., Yao, J., 2015. Numerical evaluation of passive control of VIV by small control rods. *Applied Ocean Research* 51, 93–116. doi:10.1016/j.apor.2015.03.003.